CSIRO PUBLISHING

Australian Journal of Physics

Volume 50, 1997

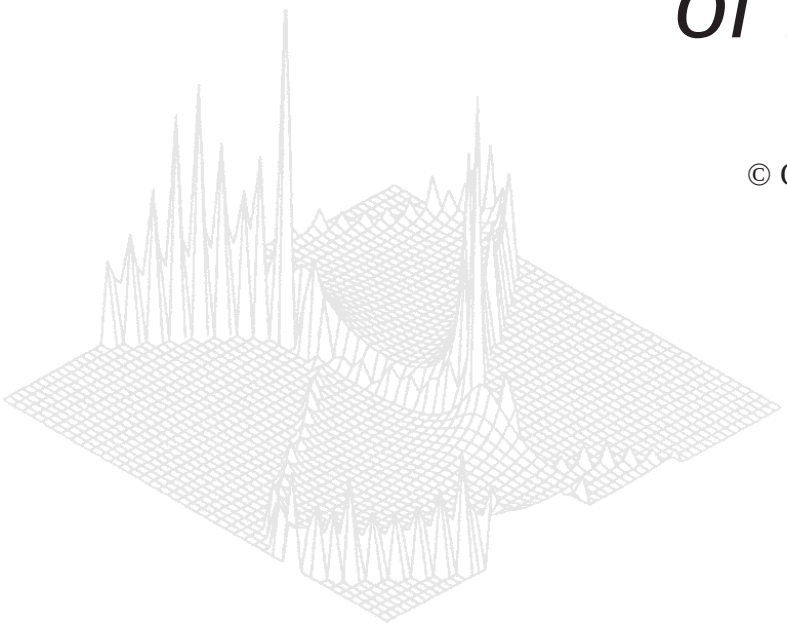

A journal for the publication of
original research in all branches of physics

www.publish.csiro.au/journals/ajp

All enquiries and manuscripts should be directed to
Australian Journal of Physics
CSIRO PUBLISHING
PO Box 1139 (150 Oxford St)
Collingwood Telephone: 61 3 9662 7626
Vic. 3066 Facsimile: 61 3 9662 7611
Australia Email: peter.robertson@publish.csiro.au

Published by **CSIRO** PUBLISHING
for CSIRO Australia and
the Australian Academy of Science

Aust. J. Phys., 1997, **50**, 827–49

Cosmic Ray Anisotropy Studies with a Small Air Shower Array

A. G. K. Smith and R. W. Clay

Department of Physics and Mathematical Physics, University of Adelaide, Adelaide, SA 5005, Australia.

Abstract

A small cosmic ray extensive air shower (EAS) array for anisotropy studies has been built and operated in the southern hemisphere for a full year. The operation of such an array is discussed as a possible prototype for a multiarray system which would be simple and reliable to operate. Data from the array are presented to add to the sparse southern hemisphere data set below energies of about 1 PeV.

1. Introduction

The majority of cosmic rays are charged particles and follow curved paths through magnetic fields in our galaxy. This means that positional astronomy is not possible except perhaps at the highest energies. At modest energies we expect that the overall cosmic ray beam will not be uniform over the sky. Any deviation from isotropy will reflect very general properties such as the motion of the solar system relative to the overall cosmic ray gas or a diffusive drift of cosmic rays from a high density source region towards a sink such as intergalactic space. It is now recognised that any anisotropies are small and that large data sets are required to make useful measurements which overcome the statistical uncertainties of counting experiments (Clay 1987).

An approach to the problem of recording many cosmic rays in an economical way is to simply record coincidences between a number of cosmic ray detectors. This was the usual technique employed many years ago (Farley and Storey 1954, 1957; Daudin *et al.* 1956). Air shower arrays were used which were simple and robust although with relatively poor angular resolution. We have built and operated a modern version of such an array to evaluate its possibilities as a prototype for a multi-array system.

The primary aim of this project was to build a low cost, low maintenance system which would collect anisotropy data for a period of at least one year with an on-time efficiency of 99% or better. The energy range under consideration was $0{\cdot}1$ to 1 PeV, for which there is currently very little southern hemisphere data available (Smith and Clay 1993). In carrying out this experiment, we have been able to acquire data which add to the sparse anisotropy data at these energies.

The prototype array was located within a building at the Thebarton Campus of the University of Adelaide (longitude 138°W, latitude 35°S, elevation 40 m), about

10.1071/PH96066 0004-9506/97/040827$10.00

four kilometres west of the main city campus. It operated almost continuously from mid-October 1992 until late February 1994.

2. Cosmic Ray Anisotropies

An apparently remarkable feature of the cosmic ray beam is that, at most energies, it is highly isotropic. Deviations from isotropy are generally less than 1%. For convenience, this deviation is usually expressed as an anisotropy, the difference between the maximum and minimum intensity divided by the sum of the maximum and minimum intensity. For practical and historical reasons, the maxima and minima are derived from a Fourier analysis of measurements of the intensity along bands of declination viewed by the detector. Thus, one derives an anisotropy amplitude and phase in right ascension at a particular declination. This is usually found from the first Fourier component in right ascension.

Clearly, this approach assumes that the deviation from isotropy is large-scale and this appears to be the case. Few specific source directions have been found in the cosmic ray beam. The anisotropy is thus likely to give information on the propagation of cosmic ray particles which is local on the scale of the particle gyro-radius in a typical galactic field. This dimension has a value of about 1 pc at 10^{15} eV.

Since the anisotropies are low, it is necessary to consider the effect on the measurement of counting statistics for a finite data set and the effect of small count rate variations associated with meteorological conditions. Counting statistics (e.g. Linsley 1975) allow the use of a convenient parameter (k_0) to characterise the anisotropy amplitude probability distribution. This is given by $Nr^2/4$ where r is the amplitude and N is the number of events used in the data set. We can set a 'noise' amplitude to be the root mean square amplitude and this occurs for $k_0 = 1$. The noise amplitude is thus $2/\sqrt{N}$ where N is the total number of events in the data set. Meteorological conditions generally have a strong effect when Fourier analysed in solar time but have a much reduced effect in sidereal time (or right ascension).

The data available on the cosmic ray anisotropy are limited in the southern hemisphere and the improvement of those data through increased samples will be a final aim of this experiment. This prototype array was designed to operate broadly in the decade of primary energies between 10^{14} and 10^{15} eV. Fig. 1 shows a compilation of data presently available around this energy range.

3. Array Hardware and Software Description

The Thebarton Array consisted of five particle detectors arranged approximately as a centred square with sides of length $11 \cdot 5$ m, the size of the square and the actual positioning of the detectors within this area being limited by the dimensions and layout of the building in which the array was constructed. The output signals from the detectors were carried via cables to a central data acquisition unit (DAU), located within the same building. Data were logged by a personal computer interfaced to the DAU. Remote access to the computer was available via a 2400 baud modem connected to a telephone outlet in the building. In this section, the array hardware and software design will be described briefly.

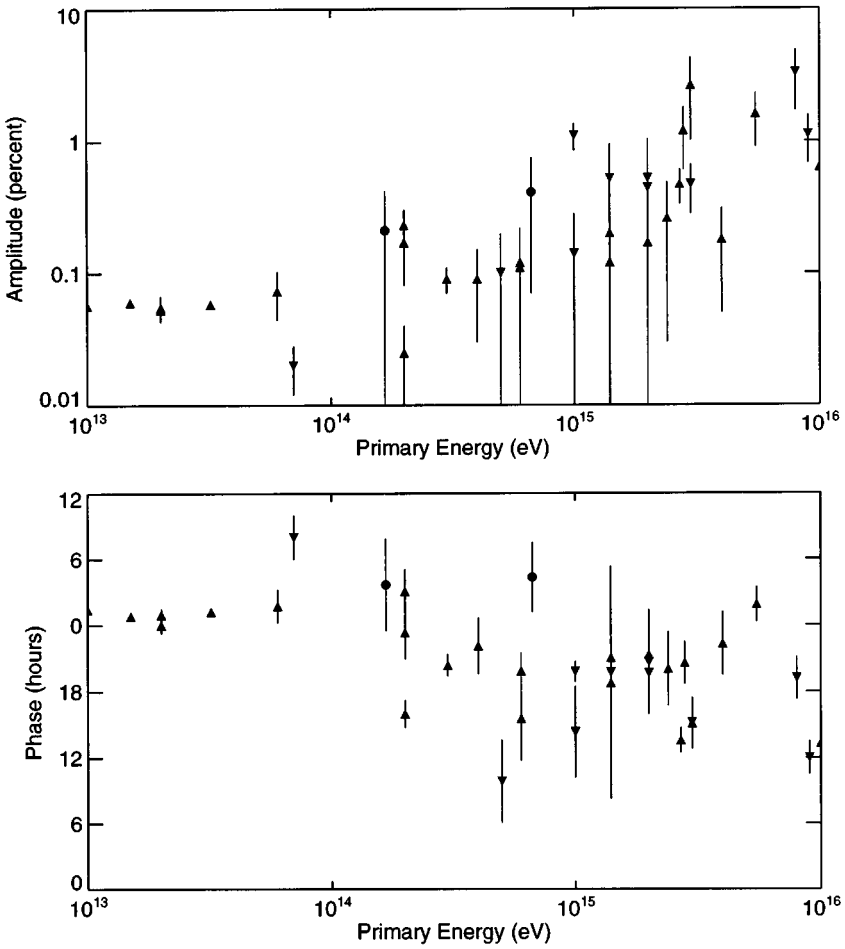

Fig. 1. Anisotropy results in the energy range 10^{13} to 10^{16} eV. Downward-pointing triangles: previous southern hemisphere results (Escobar *et al.* 1960; Farley and Storey 1954, 1957; Fenton *et al.* 1990; Gerhardy and Clay 1983). Upward-pointing triangles: previous northern hemisphere results (Alexeenko *et al.* 1981; Alexeenko and Navarra 1985; Citron and Stiller 1958; Cranshaw and Galbraith 1954; Daudin *et al.* 1956; Delvaille *et al.* 1962; Gombosi *et al.* 1975; Kifune *et al.* 1986; Krasilnikov 1960; Lloyd-Evans 1982; Nagashima *et al.* 1990; Sakakibara *et al.* 1979). Circles: results from this work.

Table 1. Thebarton Array detector layout

Dector number	Coordinates	
	x (m)	y (m)
1	−5·30	−5·65
2	+5·60	+5·65
3	−5·60	+5·65
4	+5·60	−5·60
5	+0·50	−0·95

(3a) Particle Detectors

Each detector contained a $0{\cdot}25\ m^2$ (500 mm square) by 50 mm thick slab of plastic scintillator viewed by a photomultiplier tube (RCA 8055 or Thorn EMI 9623B), inside a metal box measuring 600 by 600 by 800 mm. The inside of each detector box was coated with reflective paint. The layout of the array is given in Table 1.

The photomultiplier signals were amplified *in situ* with charge sensitive preamplifiers. Included in the same package as the preamplifier circuit was a temperature sensor, consisting of an operational amplifier and an external semiconductor probe which was taped to the outside of the detector box.

The triggering threshold for each detector was set at the $1{\cdot}5$-particle level, and the array was triggered when two or more detectors triggered within a period of one microsecond. These somewhat minimal selection criteria were chosen so as to collect as many air shower events as practicable, with the intent of applying more stringent selection criteria (i.e. increasing the thresholds and/or number of coincidences) in software during analysis.

It is possible that the array could be triggered by a chance coincidence. It was estimated that the probability of such accidental triggers was about $0{\cdot}1\%$.

(3b) Data Acquisition

When an event occurred, the DAU digitised the pulse height from each detector (regardless of whether that detector had been triggered or not), the ambient temperature at each detector, and the atmospheric pressure. The arrival time of the shower was provided by the computer's internal clock. Particle density measurements were accurate to approximately $0{\cdot}25$ particles (range 0 to 250 particles), temperatures to $0{\cdot}1$ degree Celsius, and the atmospheric pressure to 1 mbar.

It was desirable that (in order of relative importance):

(1) Data acquisition should continue uninterrupted during routine administrative tasks (such as disk management, retrieval and/or backup of data files, resetting the system clock, etc.);
(2) some limited analysis be performed in real time, aiding the rapid detection and diagnosis of major hardware problems; and
(3) the computer could be accessed remotely via a modem, so that data could be retrieved and administrative tasks performed without physically travelling out to the site, making it feasible to check the array's performance several times per day.

It was hoped that these features would help ensure a continuous data set and reduce downtime by helping to detect failures in good time. However, it was important that the computer's primary task, that of data logging, should not be significantly degraded or compromised by this extra functionality. An integrated data acquisition and remote control program, designed to run on an IBM AT-compatible personal computer under MS-DOS, was developed to provide all the above capabilities.

Data from the most current event and singles rates were displayed by the computer, and updated in real time. For events, both the raw ADC values and the processed values (based on the most current calibrations) would be shown.

In addition, the event rate (in events per minute) would be calculated every minute, based on a running mean taken over the past hour.

4. Operation of the Array

The Thebarton Array first began collecting data in mid-October 1992. Although it ran almost continuously from that time onwards, the data taken during the first few months of operation are of poor quality. Problems with the hardware and software appeared to have been solved by mid-February 1993, and after some final adjustments, the anisotropy experiment began on 1993 February 20. It ran until 1994 February 21 03:00 UTC.

The singles rates for each detector remained remarkably constant. They were found to vary mildly with temperature, with a different temperature coefficient for each detector, ranging from $-0{\cdot}4$ to $+0{\cdot}5\%$ per degree. The daily temperature variation within the building never exceeded 5°C per day, so the average daily variation in the singles rates was about $1{\cdot}3\%$. During the 366-day period of the anisotropy experiment, a total of only $2{\cdot}1$ days of data was lost or had to be completely discarded. Of this, approximately 66% resulted from hardware or software failures, 30% from loss of mains power, and the remaining 4% from deliberate shut-downs for repairs or routine maintenance. The original design goal of a yield of 99% useful data over a period of one year was therefore comfortably achieved.

An intermittent connector fault in one detector was found in early October 1993. The electrical pathway to the discriminator unit was sound, so the triggering of the array was unaffected. Prior to this, the software that was routinely used to monitor the array's performance only looked at the singles rates and the hourly event rate, neither of which were affected by the fault; it was subsequently upgraded with the addition of a program which simply added up the number of particles from each detector for each hour, and reporting if this figure was outside specified limits. The fault only affected the ability to record the pulse height from Detector Two, and had no other effect upon the experiment.

(4a) Array Livetime and Event Rate

The operating software was designed so that the exact date and time was recorded to a log file whenever the system was booted or shut-down. The time of a power failure cannot be recorded accurately because, without an uninterruptable power supply, the computer is unable to continue functioning. However, it can be estimated to better than one minute because the singles rates are written to disk every minute on the minute.

The Thebarton data set covers a total period of 31,621,007 s. The livetime, calculated in the manner described above, has an absolute lower limit of 31,440,265 s and an upper limit of 31,441,306 s, or about $31,440,800 \pm 500$ s. A total of 811,267 events was collected during this time, giving a mean event rate of one event every $38{\cdot}76$ s.

The event time-spacing distribution is graphed in Fig. 2. Since events arrive randomly in time, it is expected that this will follow an exponential distribution

$$p(t) = k \exp(-Rt)\,, \tag{1}$$

where R is the mean event rate. As can be clearly seen, the data are well fitted in this way, although there is a slight deficit in the number of events in the first bin. This deficit is much larger than would be expected from the array dead-time alone. Simulations have shown that this is largely an artifact of the limited precision of the clock (times were only recorded to the current second) and the binning process. The event rate calculated from a linear regression of the event time spacing distribution (five second bins, with the first bin excluded) gives one event every $39 \cdot 8$ s with a coefficient of correlation $R = -0 \cdot 99820$.

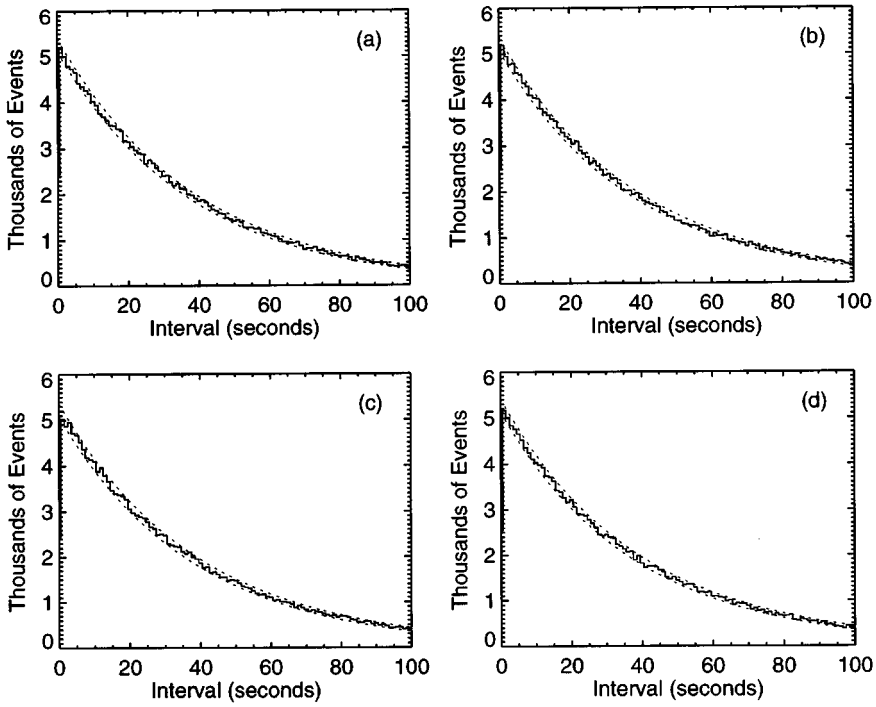

Fig. 2. Experimental event time-spacing in four different parts of the sky: (*a*) 02 to 08 hours right ascension, (*b*) 08 to 14 hours, (*c*) 14 to 20 hours, and (*d*) 20 to 02 hours. The dotted lines represent the 2σ Poisson error limits to the fitted exponential. Diagram (*a*) covers the region in which anomalies were reported by Bhat *et al.* (1979, 1980).

Bhat *et al.* (1979, 1980) reported a significant deviation from the exponential law for small time-spacings at energies above 10^{14} eV, suggesting a non-random component to the cosmic ray flux at low energies. They found an excess of event time-spacings below 25 s, apparently from a source located at a right ascension of 05 ± 03 hours. Subsequent investigations failed to confirm this result; for example, examination of the data from the Buckland Park air shower array (Clay and Gerhardy 1980; Clay and Dawson 1981) has yielded results consistent with random expectation. The results from the Thebarton Array confirm these latter findings. The observed distribution is in excellent agreement with the exponential law for all time-spacings below 100 s. This has been investigated further in Fig. 2, in which the data set has been divided up into four equal parts by sidereal time,

and the event time-spacings plotted for each. The divisions have been chosen so that the anomalous region at 05 ± 03 hours in right ascension falls within one quarter (Fig. 2*a*). No deviation is evident outside of normal statistical limits.

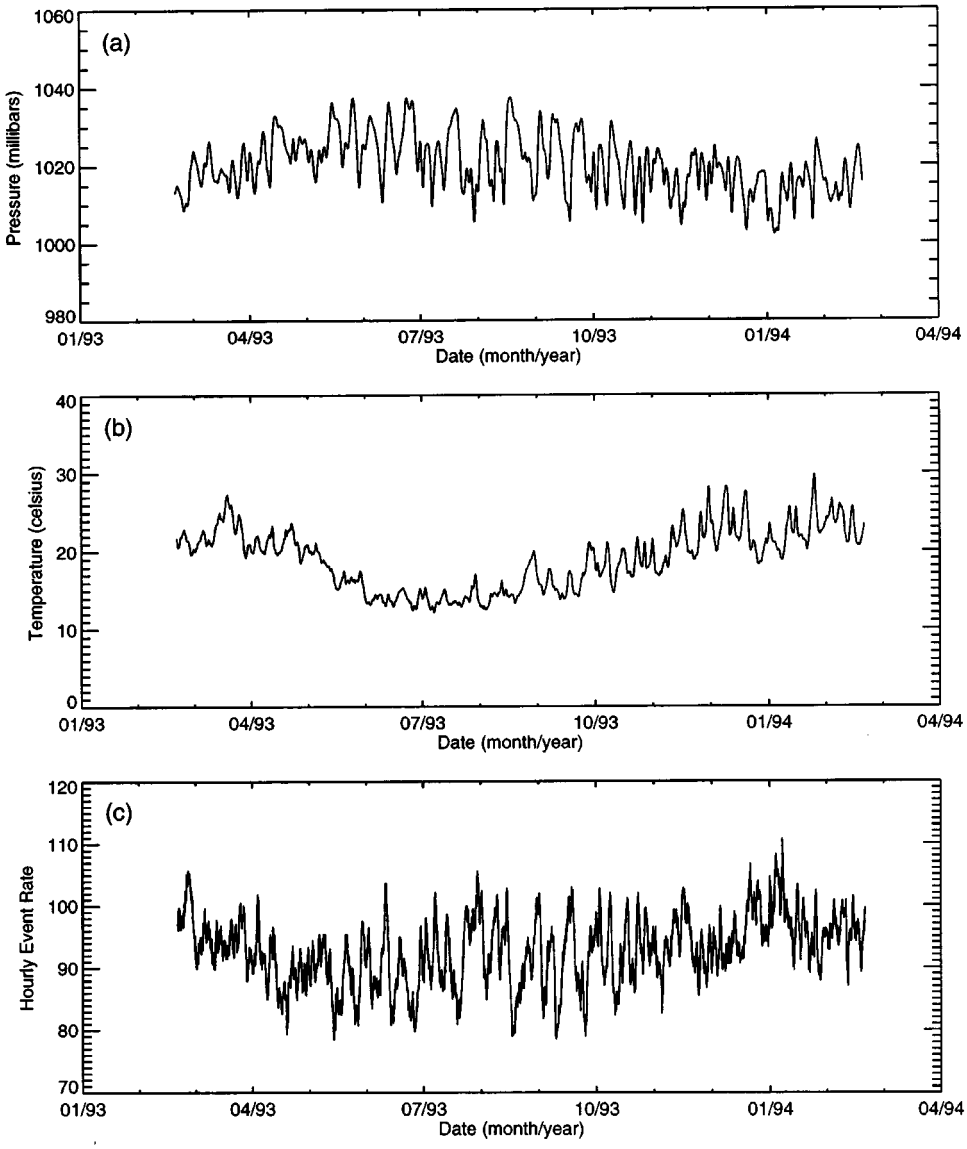

Fig. 3. Atmospheric data and hourly event rates for the Thebarton Array: (*a*) pressure, (*b*) temperature and (*c*) event rates. The data plotted are running means taken over a period of 24 hours.

(4b) Atmospheric Effects

The building in which the Thebarton Array was located has thick brick walls and a high ceiling, which provided excellent isolation from large variations in the

outside temperature, and extra thermal insulation on each of the detectors was not required. The internal temperature never varied by more than about 5°C throughout the day, even though the external temperature might have varied by up to 15°C.

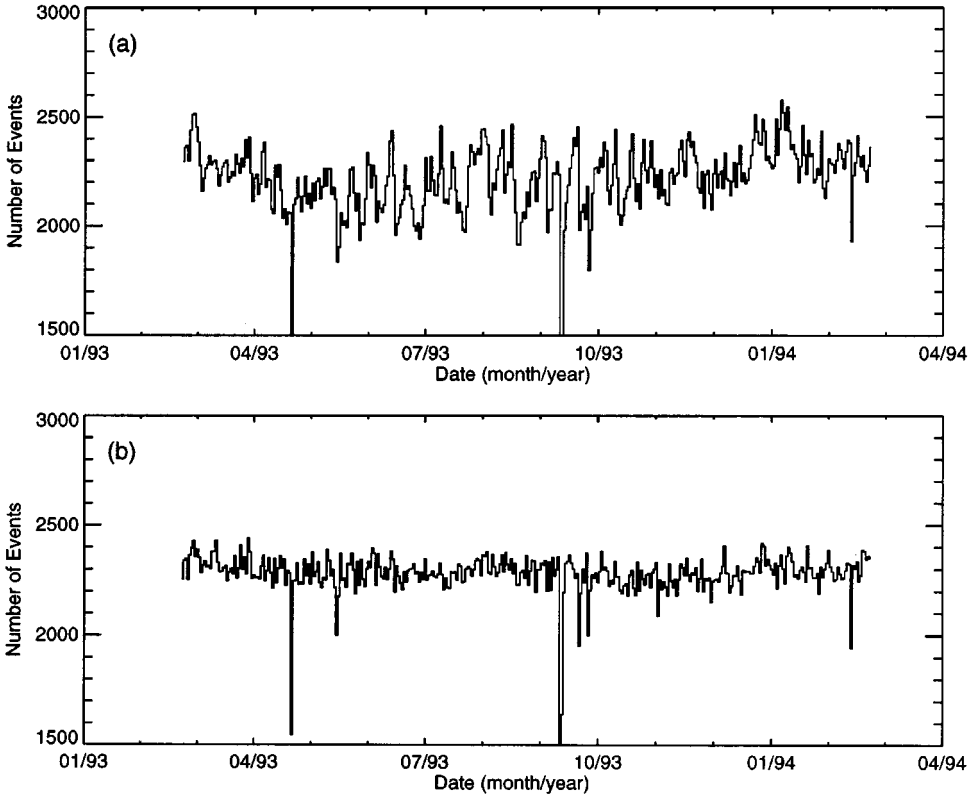

Fig. 4. Daily event rates for the Thebarton Array: (*a*) raw numbers and (*b*) after weighting for atmospheric pressure.

The barometric rate coefficient was found to be $(-7{\cdot}6 \pm 2{\cdot}2) \times 10^{-3}$ mbar^{-1}, which is in good agreement with the figure of $(-7{\cdot}2 \pm 0{\cdot}9) \times 10^{-3}$ mbar^{-1} found for our Buckland Park array (Gerhardy 1983) which covers approximately the same shower size range as the Thebarton Array. The larger error in the Thebarton result comes from the lower hourly event rate and the resulting higher statistical variations. In a multiple regression analysis of event rate against pressure and temperature, the temperature effect is found to be statistically insignificant. However, it is apparent from Fig. 3 that the event rate is correlated quite strongly with temperature. The explanation is that there is a seasonal variation in the atmospheric pressure, which gives rise to an anticorrelation between pressure and temperature. It can be seen in Fig. 4 that correction of the raw daily event rates for pressure effects alone flattens the graph, the deviations being consistent with Poisson statistics, and there is no residual temperature effect.

If either the temperature or pressure variations have Fourier components in sidereal time, spurious components may be introduced into the shower detection

rate (Farley and Storey 1954). This may occur if there is an an annual modulation of the amplitude of the variation in solar time. The amplitude and phase of the solar diurnal temperature variation are plotted as a function of date in Fig. 5. Although there is a great deal of scatter in the graph, it is evident that the amplitude varies with an annual cycle. There is a minimum of about 1°C at midwinter and a maximum of about 2·5°C at midsummer. The phase is fairly consistent with a maximum at around 18:00 hours LMST (local mean solar time), although there appears to be a phase modulation with an amplitude of about 1 hour and maximum in July. On the other hand, the amplitude and phase of the solar semidiurnal pressure variation, shown in Fig. 6, appear to remain relatively constant throughout the year; we have plotted the second harmonic rather than the first harmonic here because the former is the most prominent effect. The Fourier components of the temperature measured at Detector Two and the atmospheric pressure are given in Table 2. There is a moderate sidereal component to the temperature but, as we have seen, the effect of the ambient temperature upon the detected shower rate is negligible. The sidereal component of the atmospheric pressure is minor, and the spurious anisotropy resulting from this (approximately 0·08%) is well below the level of the noise for our experiment.

As an example of how an annual modulation of a solar diurnal variation can give rise to spurious sidereal components, consider the solar diurnal temperature

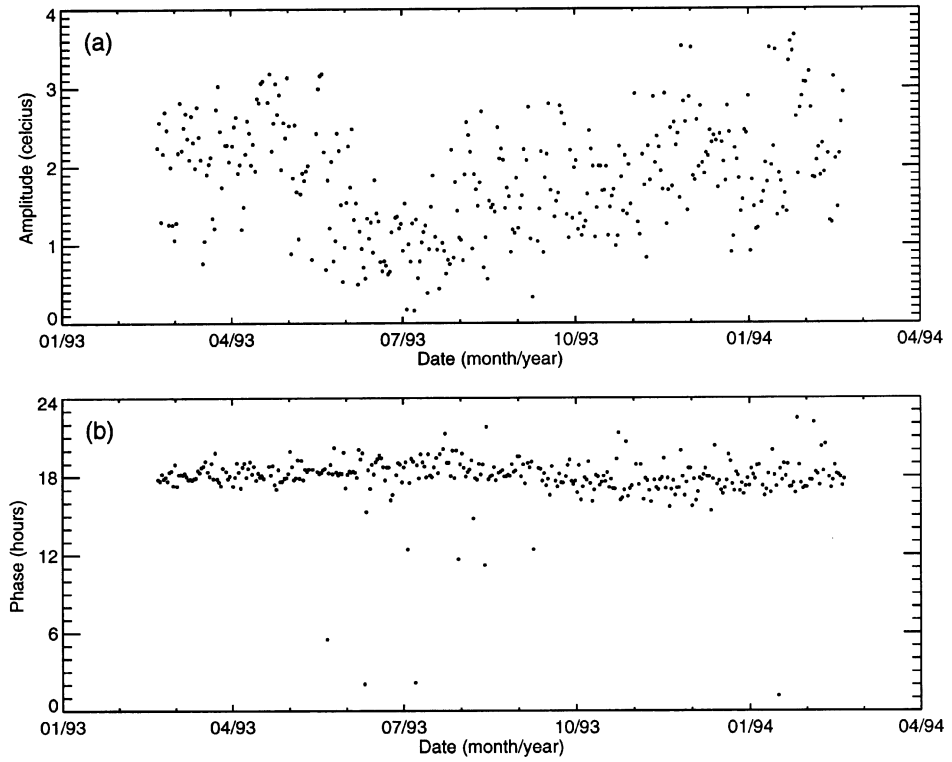

Fig. 5. First harmonic amplitude (*a*) and phase (*b*) of the solar diurnal temperature variation recorded by the sensor on Detector Two of the Thebarton Array.

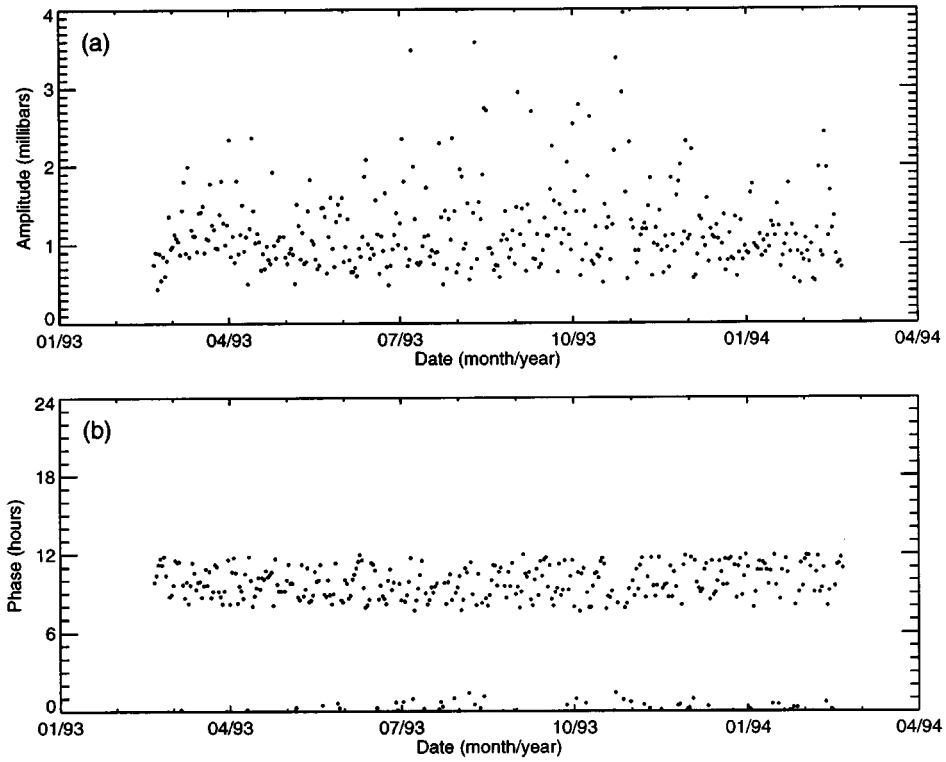

Fig. 6. Second harmonic amplitude (*a*) and phase (*b*) of the solar diurnal pressure variation recorded by the Thebarton Array.

Table 2. Fourier components of the (*a*) temperature measured at Detector Two and (*b*) atmospheric pressure

	First harmonic		Second harmonic	
	Amp (°C)	Phase (hr)	Amp (°C)	Phase (hr)
		Temperature at Detector Two		
Solar	1·77	18·04	0·30	03·13
Sidereal	0·17	01·46	0·06	04·03
Antisidereal	0·34	08·92	0·02	01·75
		(b) Atmospheric pressure		
Solar	0·60	06·42	0·91	09·33
Sidereal	0·10	19·51	0·06	09·12
Antisidereal	0·04	22·30	0·01	02·77

variation in Fig. 5*a*. Using the amplitude of this diurnal variation, the amplitude of the spurious sidereal/antisidereal component is expected (Farley and Storey 1954) to be 0·38°C (Smith 1995). This is in good agreement with the result obtained by direct Fourier analysis of the temperature time series, 0·34°C.

5. Computer Simulations

Monte Carlo simulations of the array's behaviour were of great help in both its design and in the interpretation of the experimental results. The latter point

is of particular importance because, unlike more sophisticated experiments, we were unable to determine the parameters for each individual shower.

One of the decisions in the design of the Thebarton Array was to set the hardware thresholds and coincidence requirements as low as possible and make cuts to the data at a later stage if necessary. The factors which limited the event rate were firstly, that we would be able to handle and store the amount of data generated, and secondly, that the mean time between events be much greater than the array dead-time. Simulations (Smith 1995) showed that a trigger criterion of two coincidences at the $1 \cdot 5$-particle level met these requirements comfortably, with some margin for error. The expected event rate was around 110 events per hour. The actual mean event rate, as we saw earlier in Section $4a$, turned out to be one event every $38 \cdot 76$ s, or 93 events per hour, which is in reasonable agreement with the predicted value.

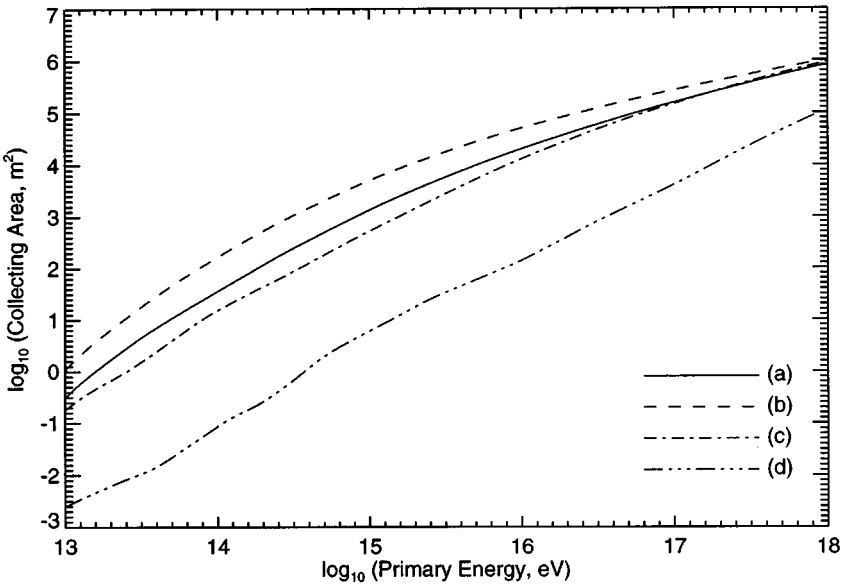

Fig. 7. Simulated collecting area for the Thebarton Array as a function of primary proton energy. Curve (a) is the average over all zenith angles between 0 and 60°, (b) for a zenith angle of 0°, (c) 45° and (d) 60°.

As the cosmic ray zenith angle θ increases, the collecting area decreases, although slowly at first (Fig. 7, curves b to d). The majority of events are detected from within about 30° of the zenith. Located at latitude 35° South, the array will receive most events from a band between declinations −65° and −5°, and about five hours of right ascension will be visible at any one time.

Even though it is not possible to determine the size of each individual shower (an energy estimator), it is possible to select shower size ranges out of the raw data during analysis in a crude way by applying cuts on the number of coincidences required and/or the triggering threshold for each detector. The simulated effects on the array shower size and energy response by making various cuts on the raw data are shown in Figs 8 and 9. In Fig. 8 the triggering threshold is held

constant at 1·5 particles while the required number of coincidences is increased, while in Fig. 9 the number of coincidences required is held at two while the detector thresholds are increased. As expected in each case, the size and energy thresholds increase while the number of usable events falls rapidly.

As mentioned previously (Section 4), reliable densities from Detector Two are unavailable for a period of several weeks due to a minor hardware fault, and if we wish to make cuts but still have a complete year of data, it is necessary

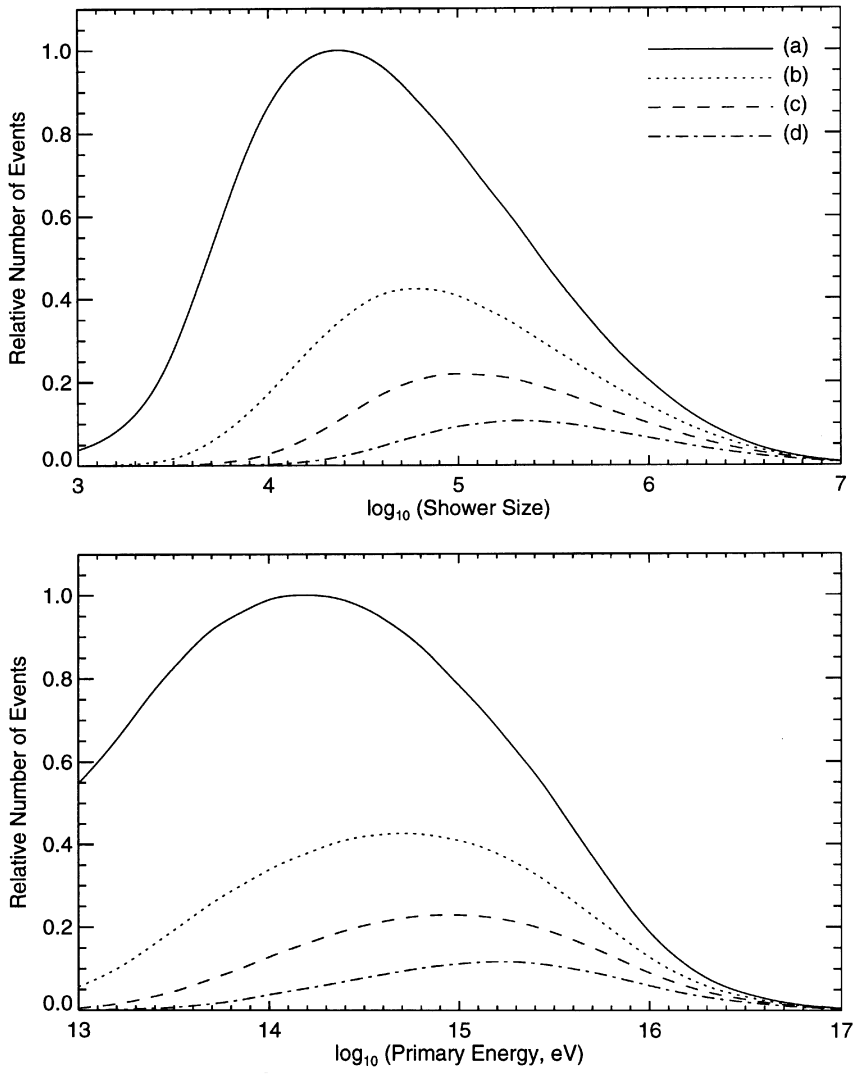

Fig. 8. Simulated shower size (above) and energy spectra (below) for the full five-detector Thebarton Array, showing the effects of applying various cuts to the raw data. In this case, the triggering threshold is held constant at 1·5 particles and the number of required coincidences is changed. Curve (*a*) shows the full data set from the hardware triggering criteria, i.e. at least two detectors at the 1·5-particle level, (*b*) the subset of events in which at least three detectors trigger at the 1·5-particle level, (*c*) at least four detectors, and (*d*) all five detectors.

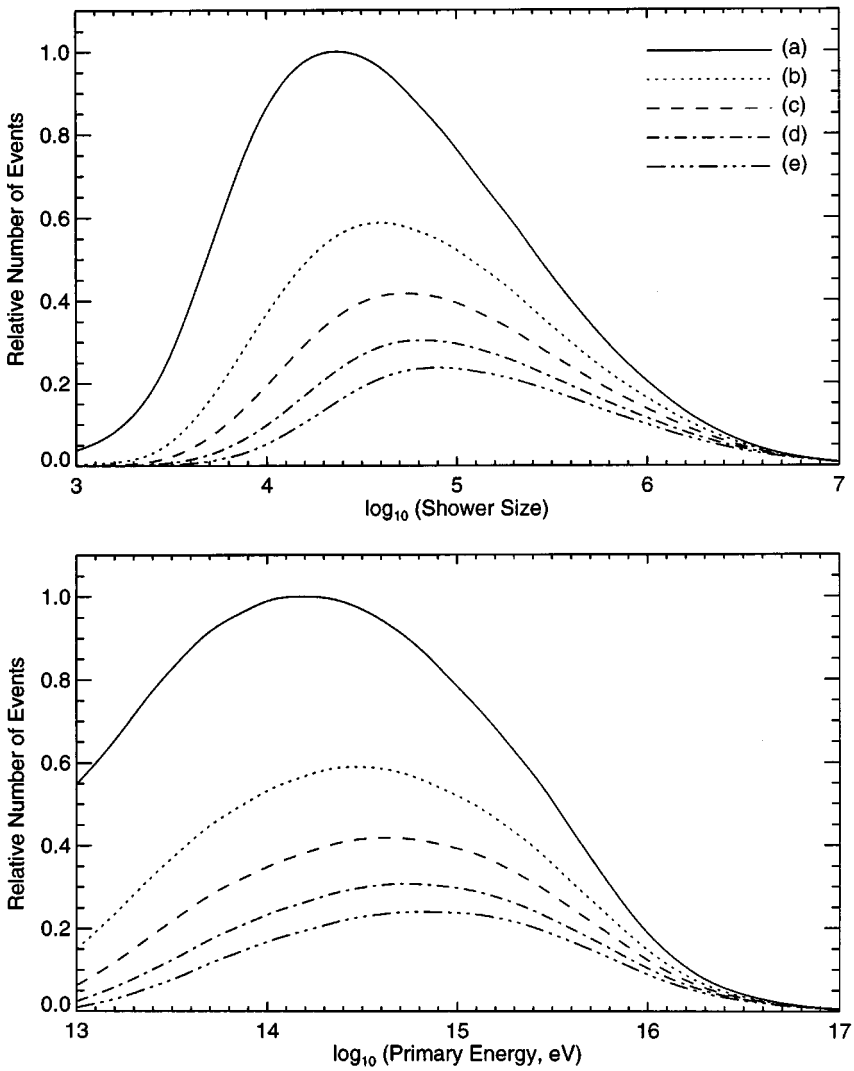

Fig. 9. Simulated shower size (above) and energy spectra (below) for the full five-detector Thebarton Array, showing the effects of applying various cuts to the raw data. In this case, the number of required coincidences is held constant at two, and the triggering threshold is changed. Curve (*a*) shows the full data set from the hardware triggering criteria, i.e. at least two detectors at the 1·5-particle level, (*b*) the subset of events in which at least two detectors trigger at the 2·0-particle level, (*c*) the 2·5-particle level, (*d*) the 3·0-particle level, and (*e*) the 3·5-particle level.

to use only data from the four-detector subarray which excludes Detector Two (hereafter, for brevity, this configuration will be referred to as '1345' and the full array as '12345'). The shape of the shower size response of the 1345 subarray is almost identical to that of the 12345 array, the major difference being that the size of the data set is reduced by about 25%.

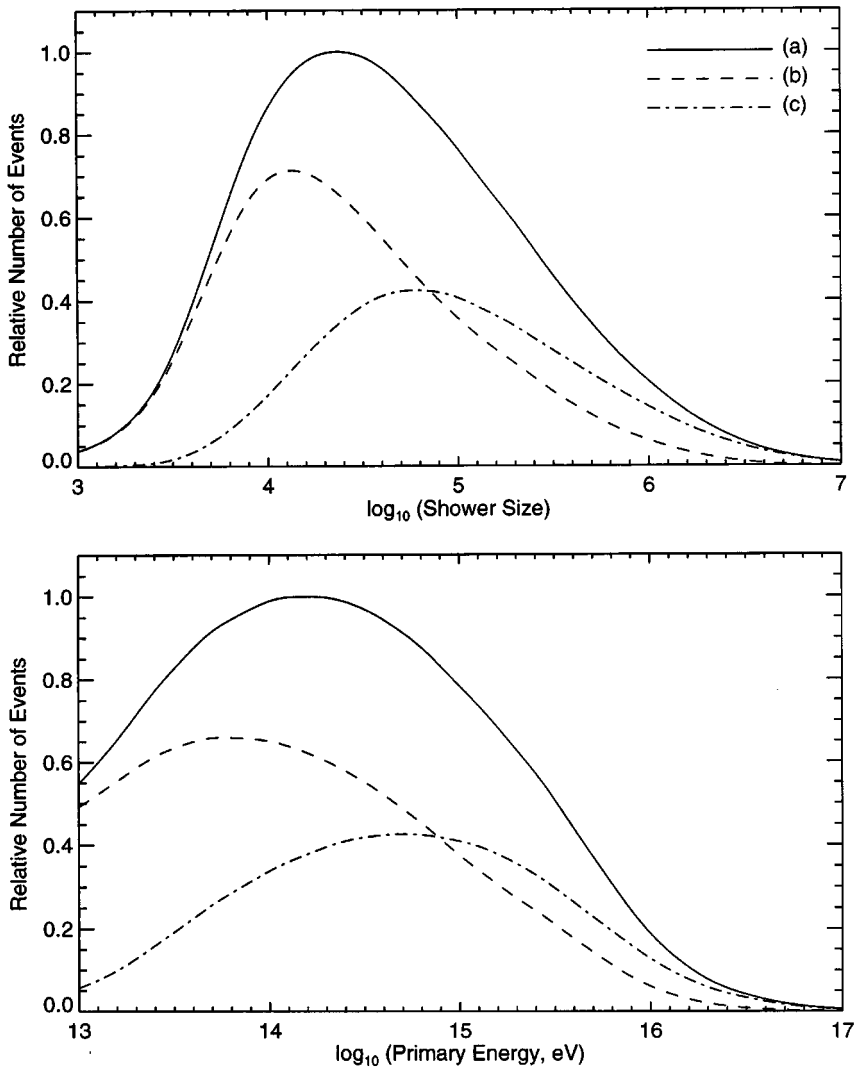

Fig. 10. Simulated shower size (above) and energy spectra (below) for the 12345 array and two subsets of the raw data. The triggering threshold is 1·5 particles and the coincidence requirements are varied. Curve (*a*) is for two or more out of the five detectors, (*b*) exactly two detectors, and (*c*) three or more detectors.

Table 3. Information about the various subsets of the Thebarton data used in this analysis, based on simulations (see also Fig. 10)

Array config.	Triggers min–max	Percent of data	Median shower size	Median primary energy
12345	2–2	60·1	$2{\cdot}37\times10^{4}$	$1{\cdot}39\times10^{14}$
	3–5	39·9	$9{\cdot}46\times10^{4}$	$5{\cdot}35\times10^{14}$
	2–5	100	$4{\cdot}18\times10^{4}$	$2{\cdot}40\times10^{14}$
1345	2–2	48·2	$2{\cdot}88\times10^{4}$	$1{\cdot}67\times10^{14}$
	3–4	28·2	$1{\cdot}19\times10^{5}$	$6{\cdot}67\times10^{14}$
	2–4	76·4	$4{\cdot}96\times10^{4}$	$2{\cdot}81\times10^{14}$

In the analysis which follows (Section 6), cuts will be applied to divide the full data set into two independent subsets which cover slightly different (although overlapping) energy ranges. We chose to apply only a minimal cut, requiring three or more coincidences at the 1·5-particle level. The conjugate of this (exactly two coincidences at the 1·5-particle level) covers a slightly lower energy range, about half a decade less on average. Simulated shower size and energy spectra for these cuts applied to the 12345 array are shown in Fig. 10 and the results summarised in Table 3. Although the results for the 12345 subarray are slightly lower than the corresponding results for the 1345 subarray, the differences (less than 0·1 decade) are, for all practical purposes, insignificant.

6. Anisotropy Analysis

As a result of the high on-time efficiency of the array and relatively few interruptions to data acquisition, the array exposure in both solar and sidereal times shown in Fig. 11 is fairly uniform. The minor dip at 09:00 LMST is the result of a number of scheduled power shutdowns. The larger dip at 13:00 LMST corresponds to the normal time at which the array was shut down for routine maintenance.

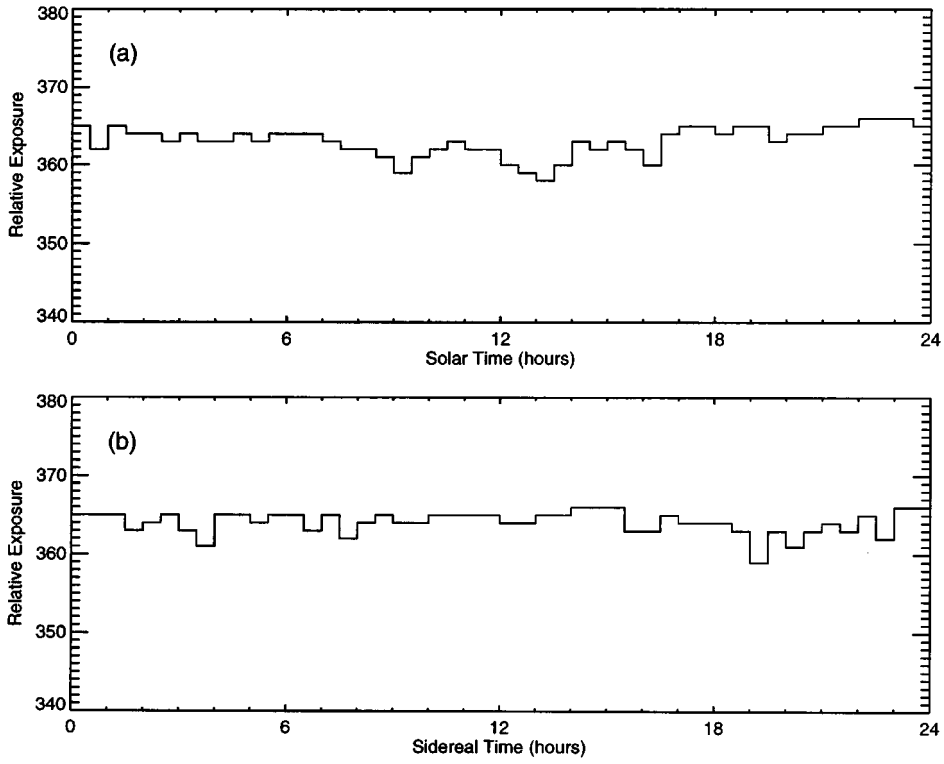

Fig. 11. Exposure of the Thebarton Array in (*a*) local mean solar time and (*b*) local sidereal time. The exposure is defined here as the number of continuous half-hour (in solar or sidereal time as appropriate) units encountered in the data set.

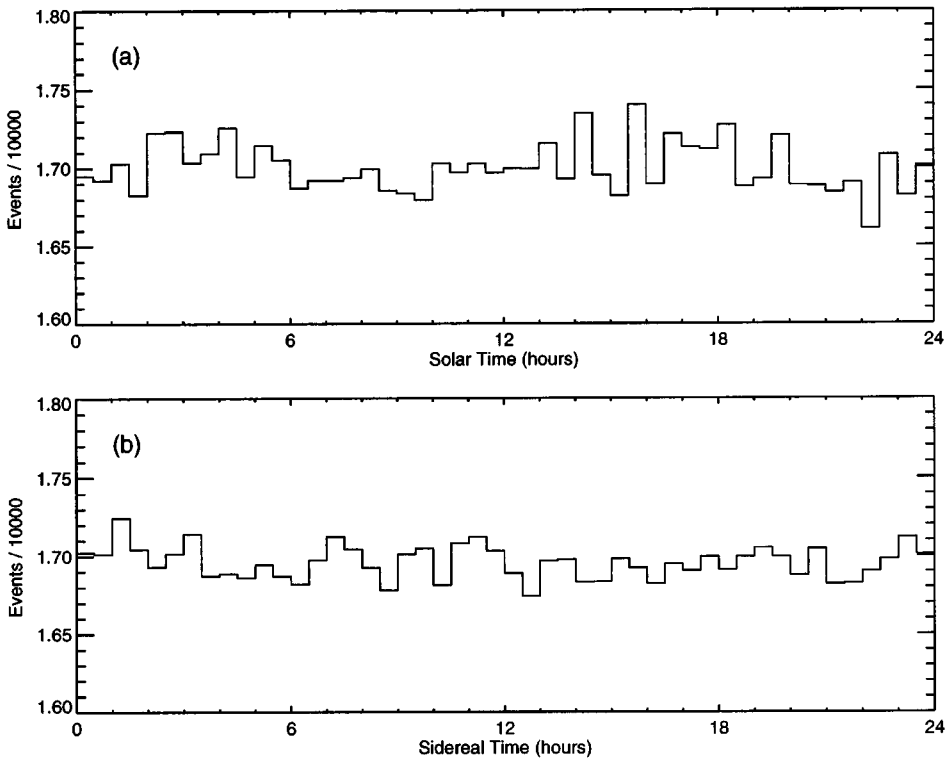

Fig. 12. Number of events detected by the Thebarton Array (weighted to eliminate exposure effects) in (a) local mean solar time and (b) local sidereal time.

The number of events detected as a function of solar and sidereal times (corrected for exposure effects) is shown in Fig. 12. The atmospheric pressure variation is clearly visible in solar time, with a second harmonic phase around 03:30 hours as we would expect. The variation in sidereal time appears to be consistent with Poisson noise at the 2σ level.

Table 4. Anisotropy results for the 12345 array for the full data set and hardware triggering

The true sidereal vectors, calculated according to the method of Farley and Storey (1954), are shown but are not necessarily meaningful at low significance levels. $1\boldsymbol{\sigma}$ errors in amplitude and phase are shown

	Number of events	First harmonic Ampl (%)	First harmonic Phase (hr)	k_0	Second harmonic Ampl (%)	Second harmonic Phase (hr)	k_0
Solar	809760	$0{\cdot}15 \pm 0{\cdot}16$	$15{\cdot}32 \pm 03{\cdot}96$	0·47	$0{\cdot}68 \pm 0{\cdot}16$	$03{\cdot}75 \pm 00{\cdot}89$	9·25
Sidereal	809840	$0{\cdot}21 \pm 0{\cdot}16$	$02{\cdot}00 \pm 02{\cdot}86$	0·89	$0{\cdot}19 \pm 0{\cdot}16$	$11{\cdot}54 \pm 03{\cdot}13$	0·74
Antisidereal	809738	$0{\cdot}20 \pm 0{\cdot}16$	$09{\cdot}06 \pm 02{\cdot}95$	0·84	$0{\cdot}03 \pm 0{\cdot}16$	$09{\cdot}17 \pm 19{\cdot}67$	0·02
Ultra-sidereal	809643	$0{\cdot}23 \pm 0{\cdot}16$	$14{\cdot}29 \pm 02{\cdot}61$	1·07	$0{\cdot}15 \pm 0{\cdot}16$	$01{\cdot}98 \pm 04{\cdot}10$	0·44
Ultra-antisidereal	809611	$0{\cdot}20 \pm 0{\cdot}16$	$04{\cdot}40 \pm 02{\cdot}97$	0·83	$0{\cdot}35 \pm 0{\cdot}16$	$01{\cdot}25 \pm 01{\cdot}70$	2·52
True sidereal		$0{\cdot}23 \pm 0{\cdot}22$	$05{\cdot}70 \pm 03{\cdot}76$	0·52	$0{\cdot}22 \pm 0{\cdot}22$	$11{\cdot}38 \pm 03{\cdot}84$	0·49
		(b) Pressure weighted:					
Solar	809760	$0{\cdot}24 \pm 0{\cdot}16$	$08{\cdot}81 \pm 02{\cdot}51$	1·16	$0{\cdot}15 \pm 0{\cdot}16$	$06{\cdot}62 \pm 03{\cdot}90$	0·48
Sidereal	809840	$0{\cdot}24 \pm 0{\cdot}16$	$00{\cdot}71 \pm 02{\cdot}53$	1·14	$0{\cdot}21 \pm 0{\cdot}16$	$11{\cdot}12 \pm 02{\cdot}87$	0·89
Antisidereal	809738	$0{\cdot}19 \pm 0{\cdot}16$	$08{\cdot}65 \pm 03{\cdot}10$	0·76	$0{\cdot}05 \pm 0{\cdot}16$	$08{\cdot}09 \pm 13{\cdot}21$	0·04
Ultra-sidereal	809643	$0{\cdot}20 \pm 0{\cdot}16$	$14{\cdot}72 \pm 02{\cdot}99$	0·81	$0{\cdot}12 \pm 0{\cdot}16$	$02{\cdot}26 \pm 04{\cdot}88$	0·31
Ultra-antisidereal	809611	$0{\cdot}20 \pm 0{\cdot}16$	$03{\cdot}22 \pm 02{\cdot}99$	0·82	$0{\cdot}35 \pm 0{\cdot}16$	$01{\cdot}14 \pm 01{\cdot}69$	2·55
True sidereal		$0{\cdot}38 \pm 0{\cdot}22$	$23{\cdot}04 \pm 02{\cdot}23$	1·47	$0{\cdot}21 \pm 0{\cdot}22$	$11{\cdot}93 \pm 03{\cdot}97$	0·46

Table 5. Anisotropy results for the 12345 array for the incomplete year and various coincidence requirements (all at the 1·5-particle level)

	Number of events	First harmonic Ampl (%)	First harmonic Phase (hr)	k_0	Second harmonic Ampl (%)	Second harmonic Phase (hr)	k_0
Solar	711611	0·19 ± 0·17	16·71 ± 03·41	0·63	0·71 ± 0·17	03·69 ± 00·90	8·98
Sidereal	711641	0·23 ± 0·17	02·93 ± 02·80	0·93	0·22 ± 0·17	11·13 ± 02·93	0·85
Antisidereal	711632	0·15 ± 0·17	06·88 ± 04·41	0·38	0·09 ± 0·17	11·21 ± 07·52	0·13
Ultra-sidereal	711579	0·35 ± 0·17	14·73 ± 01·85	2·12	0·08 ± 0·17	01·17 ± 08·19	0·11
Ultra-antisidereal	711558	0·28 ± 0·17	04·39 ± 02·28	1·40	0·36 ± 0·17	01·64 ± 01·77	2·34
True sidereal		0·09 ± 0·24	03·58 ± 10·61	0·07	0·29 ± 0·24	10·33 ± 03·17	0·73
		(b) Exactly two coincidences:					
Solar	477051	0·37 ± 0·20	18·17 ± 02·11	1·64	0·88 ± 0·20	03·45 ± 00·89	9·23
Sidereal	477045	0·24 ± 0·20	23·93 ± 03·22	0·70	0·23 ± 0·20	11·55 ± 03·41	0·63
Antisidereal	477049	0·24 ± 0·20	05·78 ± 03·20	0·72	0·04 ± 0·20	03·34 ± 19·93	0·02
Ultra-sidereal	477029	0·42 ± 0·20	15·34 ± 01·87	2·09	0·12 ± 0·20	11·41 ± 06·31	0·18
Ultra-antisidereal	476986	0·10 ± 0·20	03·61 ± 07·54	0·13	0·36 ± 0·20	01·58 ± 02·20	1·51
True sidereal		0·37 ± 0·29	21·23 ± 02·98	0·82	0·25 ± 0·29	00·07 ± 04·40	0·38
		(c) Three or more coincidences:					
Solar	234560	0·31 ± 0·29	09·07 ± 03·62	0·56	0·45 ± 0·29	04·73 ± 02·50	1·17
Sidereal	234596	0·49 ± 0·29	05·95 ± 02·28	1·41	0·23 ± 0·29	10·27 ± 04·82	0·31
Antisidereal	234583	0·15 ± 0·29	13·85 ± 07·66	0·12	0·31 ± 0·29	10·80 ± 03·60	0·56
Ultra-sidereal	234550	0·25 ± 0·29	12·50 ± 04·49	0·36	0·22 ± 0·29	03·41 ± 05·12	0·28
Ultra-antisidereal	234572	0·65 ± 0·29	04·64 ± 01·73	2·45	0·38 ± 0·29	01·74 ± 02·96	0·83
True sidereal		0·36 ± 0·41	06·59 ± 04·35	0·39	0·54 ± 0·41	10·49 ± 02·92	0·86

Table 6. Anisotropy results for the 1345 array for the full year and various coincidence requirements (all at the 1·5-particle level)

	Number of events	First harmonic Ampl (%)	First harmonic Phase (hr)	k_0	Second harmonic Ampl (%)	Second harmonic Phase (hr)	k_0
Solar	560633	0·10 ± 0·19	09·91 ± 07·09	0·15	0·71 ± 0·19	03·96 ± 01·01	7·14
Sidereal	560671	0·27 ± 0·19	03·97 ± 02·71	0·99	0·28 ± 0·19	11·70 ± 02·55	1·13
Antisidereal	560611	0·12 ± 0·19	05·25 ± 06·18	0·19	0·20 ± 0·19	00·08 ± 03·54	0·58
Ultra-sidereal	560505	0·31 ± 0·19	14·19 ± 02·36	1·31	0·14 ± 0·19	02·39 ± 05·28	0·26
Ultra-antisidereal	560532	0·46 ± 0·19	05·13 ± 01·57	2·96	0·32 ± 0·19	02·09 ± 02·24	1·46
True sidereal		0·38 ± 0·27	03·54 ± 02·70	1·00	0·25 ± 0·27	02·68 ± 04·15	0·42
		(b) Exactly two coincidences:					
Solar	391459	0·10 ± 0·23	04·11 ± 08·44	0·10	0·96 ± 0·23	03·99 ± 00·90	9·08
Sidereal	391469	0·21 ± 0·23	03·65 ± 04·21	0·41	0·32 ± 0·23	11·80 ± 02·72	0·99
Antisidereal	391447	0·29 ± 0·23	05·09 ± 03·03	0·80	0·25 ± 0·23	00·61 ± 03·48	0·60
Ultra-sidereal	391379	0·31 ± 0·23	14·71 ± 02·80	0·93	0·08 ± 0·23	10·97 ± 11·51	0·06
Ultra-antisidereal	391384	0·49 ± 0·23	04·15 ± 01·75	2·38	0·38 ± 0·23	02·48 ± 02·29	1·39
True sidereal		0·09 ± 0·32	13·91 ± 14·11	0·04	0·32 ± 0·32	02·88 ± 03·87	0·49
		(c) Three or four coincidences:					
Solar	169174	0·40 ± 0·34	12·31 ± 03·27	0·68	0·14 ± 0·34	03·52 ± 09·31	0·08
Sidereal	169202	0·41 ± 0·34	04·33 ± 03·20	0·71	0·21 ± 0·34	11·33 ± 06·28	0·19
Antisidereal	169164	0·27 ± 0·34	16·86 ± 04·79	0·32	0·20 ± 0·34	10·35 ± 06·50	0·17
Ultra-sidereal	169126	0·32 ± 0·34	13·01 ± 04·12	0·43	0·52 ± 0·34	03·02 ± 02·53	1·14
Ultra-antisidereal	169148	0·51 ± 0·34	07·44 ± 02·57	1·10	0·28 ± 0·34	00·76 ± 04·71	0·33
True sidereal		0·32 ± 0·49	01·55 ± 05·77	0·22	0·39 ± 0·49	10·04 ± 04·80	0·32

The results from Fourier analyses of the data are given in Tables 4, 5 and 6. The first of these (Table 4) gives the results from the full year of data with no cuts (i.e. hardware coincidence), both with and without pressure corrections. All harmonics, with the exception of the second harmonic in solar time, are consistent with noise. As we have found in data sets from other experiments, the pressure corrections do not make much difference to the final results except that the amplitude of the second harmonic of the anisotropy in solar time is considerably reduced in significance. We see that pressure corrections are of little value and we shall now dispense with them.

Tables 5 and 6 show the results obtained by applying the cuts given in Table 3. Before cuts can be applied to the data set from the full (12345) array, we must first cut out the data from the period when reliable densities are unavailable for Detector Two. This reduces our data set slightly, and introduces a gap of several weeks into the middle. If we first analyse the data without any cuts as in Table 5*a*, we can compare the results with those obtained previously in Table 4*a*. The two agree within experimental error. In Table 6 we go through the same process for the 1345 subarray, only this time we have an unbroken year of data, although with a reduced event rate. The energy ranges covered by the different cuts to the data from the 12345 and 1345 arrays are very similar, and so the results can be compared directly; that is (*a*), (*b*) and (*c*) in Table 5 can be compared directly with their counterparts in Table 6. The two sets of results are in complete agreement (within experimental error) in the amplitude and phase of all components. The 'true sidereal' anisotropies were calculated by the method of Farley and Storey (1954). However, the quantities from which they are derived are themselves of low statistical significance.

The Fourier amplitude spectra for the first and second harmonics of the full data set are shown in Fig. 13. The only Fourier component that can be said,

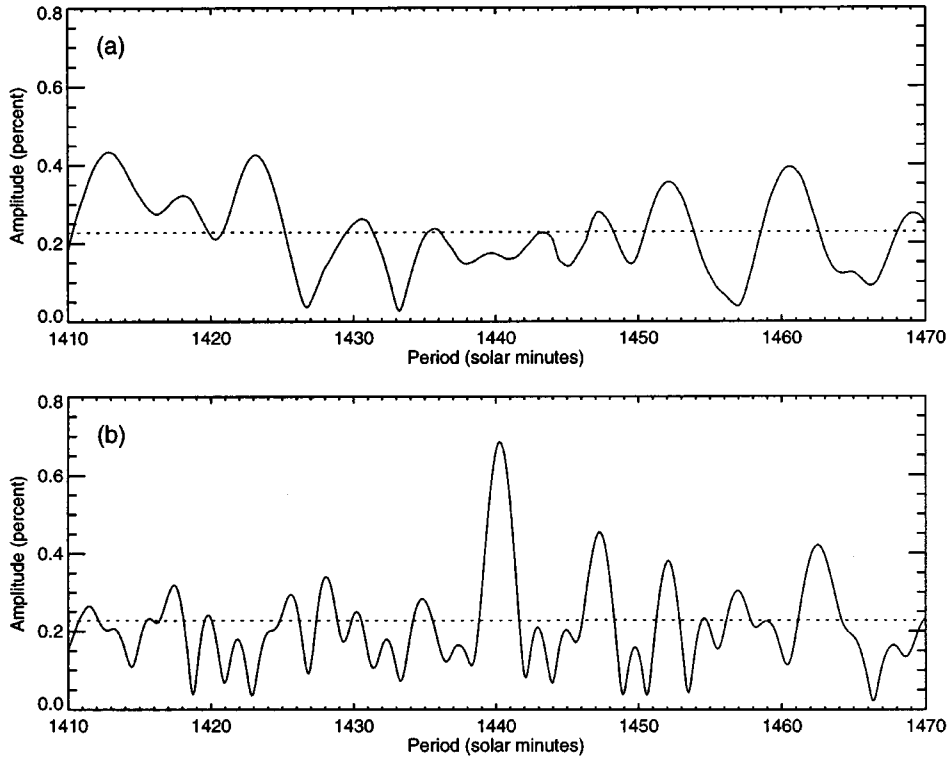

Fig. 13. Fourier amplitude spectra of the (*a*) first harmonic and (*b*) second harmonic of the Thebarton data, for periods in the region of one solar day (1440 minutes). The dotted lines represent the RMS 'noise' level.

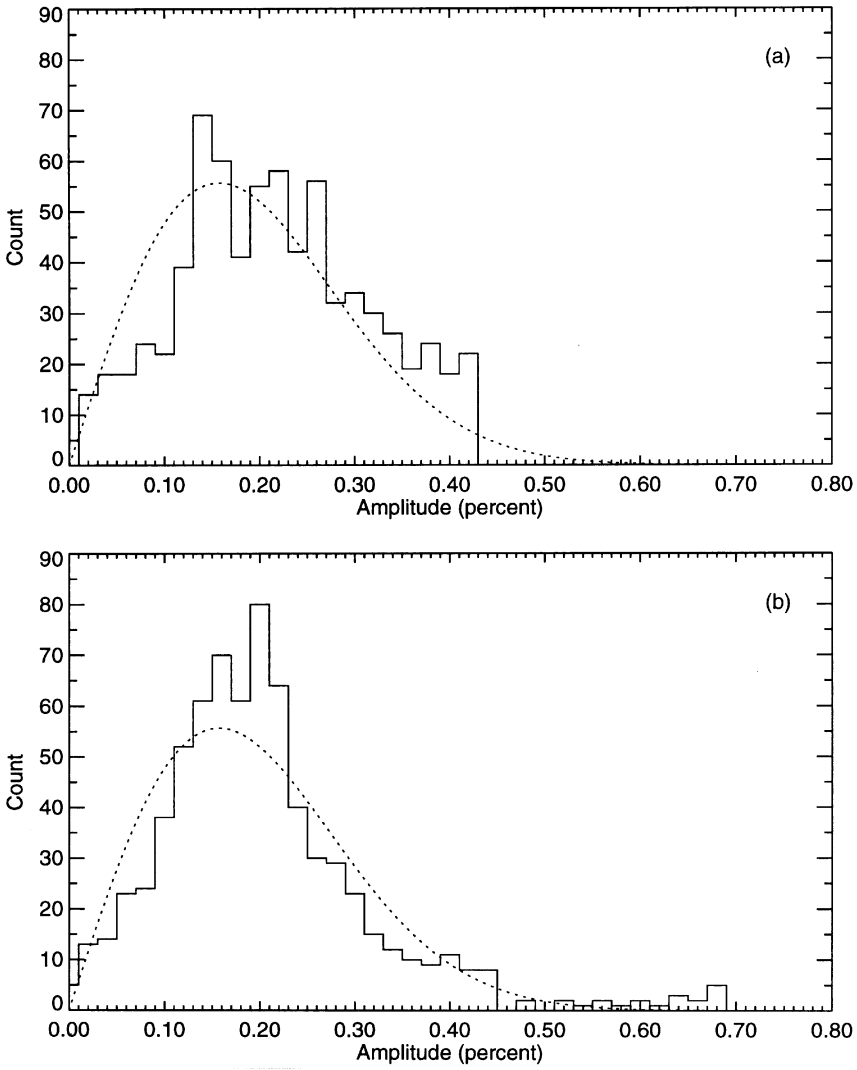

Fig. 14. Distribution of Fourier amplitudes from Fig. 13, for the (*a*) first harmonic and (*b*) second harmonic. The broken curve is that which is expected from a random data set according to Rayleigh statistics.

with any certainty, to be present is the second harmonic peak at one solar day. There are suggestions of peaks at the solar and sidereal periods, but they are of low statistical significance. The distributions of Fourier amplitudes are plotted in Fig. 14, in which it can be seen that there is good agreement with the distribution expected from a random data set.

Fig. 15 shows Fourier amplitude spectra for three randomly-generated data sets with similar characteristics to those of the real Thebarton data set, i.e. approximately $8 \cdot 1 \times 10^5$ events spanning a total of $365 \cdot 25$ solar days and an event time-spacing drawn from an exponential distribution with a mean of $38 \cdot 76$ s. These diagrams illustrate two important points. Firstly, variations in amplitude

as a function of frequency do not necessarily indicate the presence of either a true extraterrestrial anisotropy or of atmospheric modulations to the detected flux. Secondly, each of these show apparently significant anisotropies ($r > r_{\rm rms}$ or $k_0 > 1$) at both the solar and sidereal periods. If one were to blindly carry out a Fourier analysis at only these frequencies one might be tempted to conclude that these data sets show evidence of anisotropy.

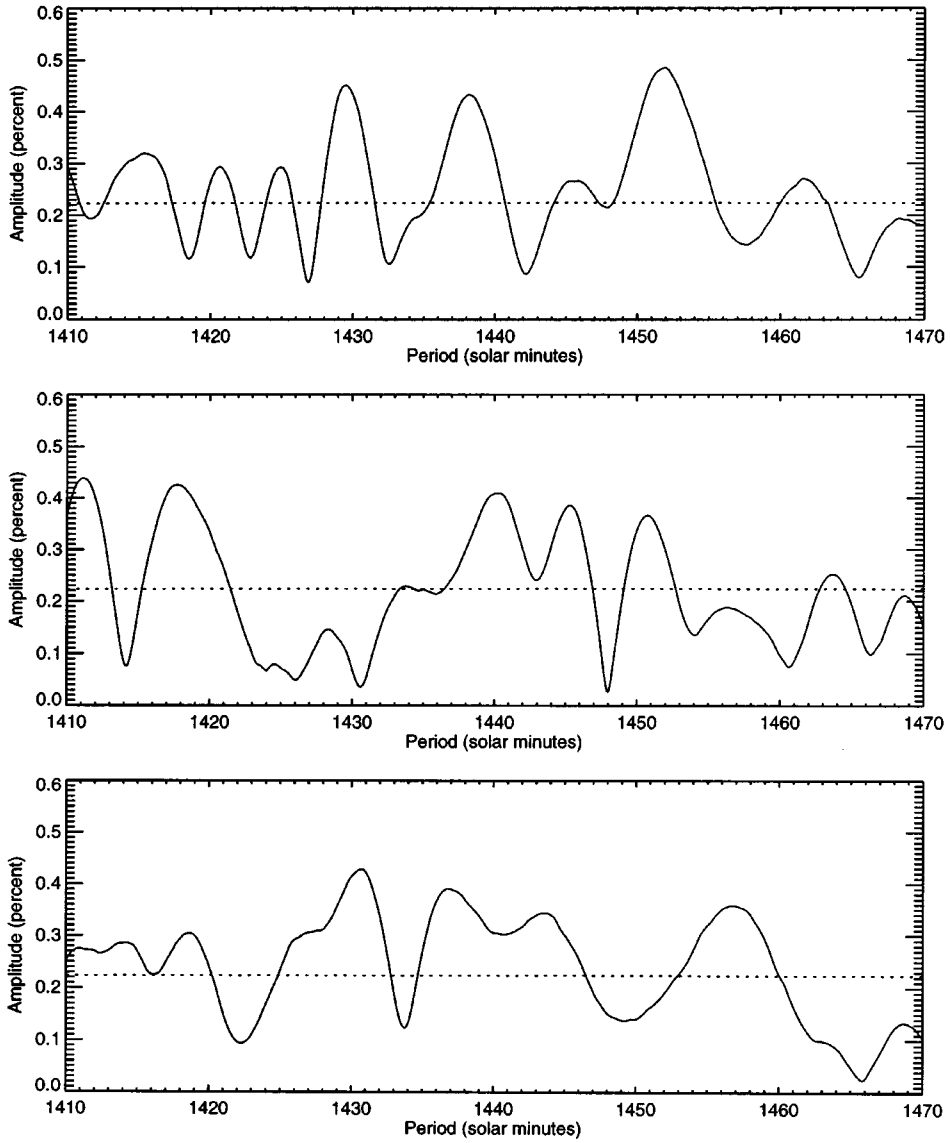

Fig. 15. Fourier amplitude spectra for three randomly-generated data sets with similar characteristics to the experimental Thebarton data set (see text for details). The solid curve shows the amplitude of the first harmonic for periods in the region of one solar day (1440 minutes) and the dotted line represents the RMS 'noise' level.

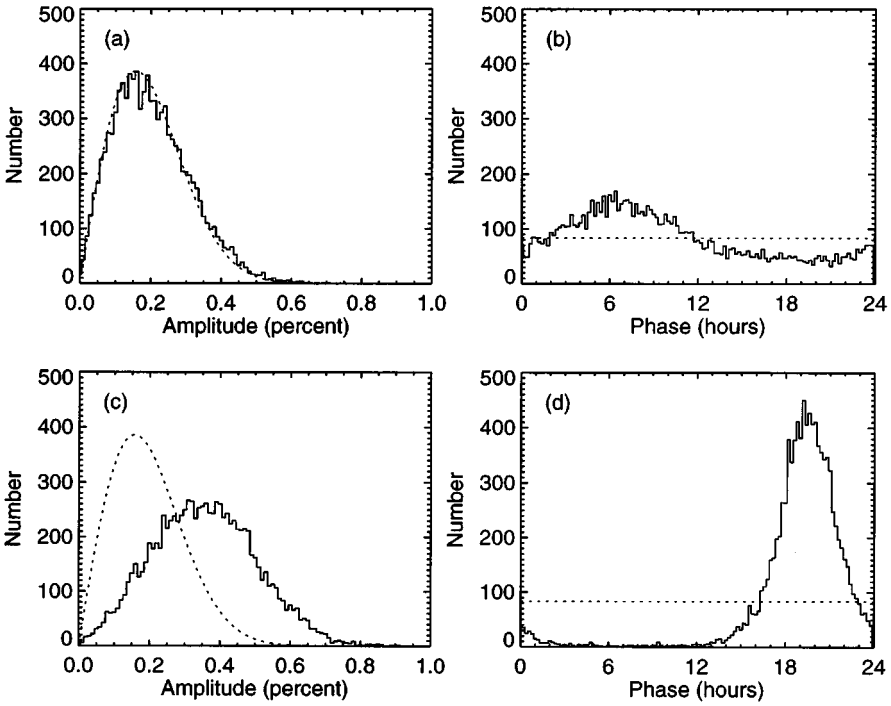

Fig. 16. Results from 10,000 simulated data sets with an event rate which varies as a function of atmospheric pressure (see text for details). Graphs (*a*) and (*b*) show the distributions of sidereal first harmonic amplitude and phase respectively, while (*c*) and (*d*) show the distributions of solar first harmonic amplitude and phase. The broken curves show the results expected from a purely random data set with a constant event rate equal to the mean event rate.

Further simulations were carried out to investigate the effect of atmospheric pressure variations upon the derived values of r and θ, the amplitude and phase of the derived anisotropy. A series of random data sets was generated as before, except that the event rate was varied as a function of atmospheric pressure. The atmospheric pressure variations were derived from readings taken by the weather station at Adelaide Airport during 1993. The event rate was calculated using the rate versus pressure relationship determined from the experiment. First harmonic solar and sidereal anisotropies were calculated for 10^4 such data sets, and the resulting distributions of these quantities are shown in Fig. 16. The sidereal amplitude distribution is indistinguishable from that expected from a random data set but, interestingly, the phase distribution shows a bias towards about 6 to 7 hours LST, with phases in the range 0 to 12 hours more than twice as likely to occur as phases in the range 12 to 24 hours. On the other hand, the solar amplitude distribution differs quite significantly from random expectation, and the phase distribution shows a very strong peak at around 19 hours LMST. These results can be compared with the harmonic analysis given in Table 2*b*, which is based upon the same atmospheric pressure data. The Fourier components of the solar variation are much stronger than the sidereal components, so we would expect the sidereal distributions in Fig. 16 to be closer to that of a random data

set. The phases of the Fourier components from Table 2*b* are consistent with the maxima of the distributions in Fig. 16 (i.e. there is a difference of 12 hours).

Figs 16*a* and 16*b* seem to imply that even though the amplitude of an anisotropy may be buried in the noise, useful information may still be contained within the phase. However, this argument applies also to atmospheric-induced variations in the observed flux. Atmospheric effects can, in principle, be removed by weighting the events according to the ambient atmospheric conditions, provided that measurements of sufficient accuracy and precision are available. Attempting to weight the data with measurements which are inaccurate and/or imprecise may simply add noise to the data. For example, Table 2*b* shows that the first harmonic of the sidereal pressure variation is $0{\cdot}1$ mbar, which is of the same order as the precision of the best atmospheric pressure measurements available to us (also $0{\cdot}1$ mbar).

Fig. 1 includes the results from the anisotropy analysis (Table 5), together with previously available anisotropy data. It is evident that, as we expect, the exposure of the array was not sufficient to reach the levels of anisotropies found in a number of other studies at these energies. On the other hand, most of those studies were in the northern hemisphere and little information was available in the south. The phases we have determined for the anisotropy are apparently consistent with other data despite the limitations of the data set.

7. Conclusions

We have built and operated for one full year a small cosmic ray air shower array designed to be robust and simple to operate. The array ran within its design goals for operational efficiency and has served as a successful pilot array for anisotropy studies at energies in the decade below 1 PeV.

In analysing the data set, we have studied appropriate analysis techniques to allow for environmental effects and find then that there is no compelling evidence to suggest that the Thebarton data set differs significantly from random expectation. The amplitude of the first harmonic sidereal variation is small and consistent with noise, but the phase, broadly between about 0 and 6 hours right ascension, is in reasonable agreement with previous results in the energy range from 10^{14} to 10^{15} eV. However, the phase could be affected by a remaining contribution due to atmospheric pressure variations, and so should be treated with caution.

Acknowledgment

This work was supported by the Australian Research Council.

References

Alexeenko, V. V., Chudakov, A. E., Gulieva, E. N., and Sborshikov, V. G. (1981). Proc. 17th Int. Cosmic Ray Conf. (Paris), Vol. 2, p. 146.

Alexeenko, V. V., and Navarra, G. (1985). *Lett. Nuovo Cimento* **42**, 321.

Bhat, C. L., Sapru, M. L., and Kaul, C. L. (1980). *Nature* **288**, 146.

Bhat, C. L., Sarma, P. R., Sapru, M. L., and Kaul, C. L. (1979). Proc. 16th Int. Cosmic Ray Conf. (Kyoto), Vol. 8, p. 57.

Citron, A., and Stiller, G. (1958). *Nuovo Cim. Suppl.* **8**, 675.

Clay, R. W. (1987). *Aust. J. Phys.* **40**, 423.

Clay, R. W., and Dawson, B. R. (1981). *Aust. J. Phys.* **34**, 591.

Clay, R. W., and Gerhardy, P. R. (1980). *Aust. J. Phys.* **33**, 753.
Cranshaw, T. E., and Galbraith, W. (1954). *Phil. Mag.* **45**, 1109.
Daudin, J., *et al.* (1956). *Nuovo Cimento* **3**, 1017.
Delvaille, J., Kandziorski, F., and Greisen, K. (1962). *Phys. Soc. Japan* **17** (Suppl. A3), 76.
Escobar, I., Nerurkar, N., and Weil, R. (1960). *Planet. Sp. Sci.* **2**, 187.
Farley, F. J. M., and Storey, J. R. (1954). *Proc. Phys. Soc.* A **67**, 996.
Farley, F. J. M., and Storey, J. R. (1957). *Proc. Phys. Soc.* B **70**, 840.
Fenton, A. G., Fenton, K. B., Humble, J. E., Bolton, K., Jacklyn, R. M., Duldig, M. L., Murakami, K., Fujii, Z., Yamada, T., Sakakibara, S., Fujimoto, K., Ueno, H., and Nagashima, K. (1990). Proc. 21st Int. Cosmic Ray Conf. (Adelaide), Vol. 3, p. 177.
Gerhardy, P. R. (1983). PhD Thesis, University of Adelaide.
Gerhardy, P. R., and Clay, R. W. (1983). *J. Phys.* G **9**, 1279.
Gombosi, T., Kóta, J., Somogyi, A. J., Varga, A., Betev, B., Katsarski, L., Kavloakov, S., and Khirov, I. (1975). Proc. 14th Int. Cosmic Ray Conf. (Munich), Vol. 2, p. 586.
Kifune, T., Hara, T., Hatano, Y., Hayashida, N., Kamata, K., Nagano, M., Nishijimi, K., Tanahashi, G., and Teshima, M. (1986). *J. Phys.* G **12**, 129.
Krasilnikov, D. D. (1960). Proc. 6th Int. Cosmic Ray Conf. (Moscow), Vol. 4, p. 271.
Linsley, J. (1975). *Phys. Rev. Lett.* **34**, 1530.
Lloyd-Evans, J. (1982). PhD Thesis, University of Leeds.
Nagashima, K., Fujimoto, K., Sakakibara, S., Fujii, Z., Ueno, H., Murakami, K., and Morishita, I. (1990). Proc. 21st Int. Cosmic Ray Conf. (Adelaide), Vol. 3, p. 180.
Sakakibara, S., Ueno, H., Fujimoto, K., Fujii, Z., Kondo, I., and Nagashima, K. (1979). Proc. 16th Int. Cosmic Ray Conf. (Kyoto), Vol. 4, p. 216.
Smith, A. G. K. (1995). PhD Thesis, University of Adelaide.
Smith, A. G. K., and Clay, R. W. (1993). Proc. 23rd Int. Cosmic Ray Conf. (Calgary), Vol. 2, p. 73.

Manuscript received 13 June, accepted 9 December 1996